Robust Nanoporous NiMn oxide Electrocatalysts for Oxygen Evolution Reaction through Defect Engineering

Journal:	*Journal of Materials Chemistry A*
Manuscript ID	TA-ART-04-2024-002679.R3
Article Type:	Paper
Date Submitted by the Author:	20-Jul-2024
Complete List of Authors:	Thomas, Arpit; Shiv Nadar University Kumar, Ambrish ; Shiv Nadar University Sharma, Ram; University of Petroleum and Energy Studies Buck, Edgar; Pacific Northwest National Laboratory, Energy and Environment Directorate Gwalani, Bharat; North Carolina State University at Raleigh Bhogra, Meha; Shiv Nadar University Arora, Harpreet; Shiv Nadar University, Mechanical Engineering

Robust Nanoporous NiMn oxide Electrocatalysts for Oxygen Evolution Reaction through Defect Engineering

Arpit Thomas[a], Ambrish Kumar[a], Ram K. Sharma[b], Edgar C. Buck[c], Bharat Gwalani[d], Meha Bhogra[a,#], Harpreet Singh Arora[a, #]

[a] Department of Mechanical Engineering, Shiv Nadar Institution of Eminence, Deemed to be University, India (UP)- 201310
[b]Centre for Inter-Disciplinary Research and Innovation, University of Petroleum and Energy Studies, Bidholi Via-Prem Nagar, Dehradun-248007
[c]Pacific Northwest National Laboratory, Richland, Washington99354, United States
[d]Department of Materials Science and Engineering, North Carolina State University, Raleigh, North Carolina 27695, United States
[#]Corresponding authors' E-mail: harpreet.arora@snu.edu.in; meha.bhogra@snu.edu.in

Abstract
The sluggish oxygen evolution reaction (OER) remains a major bottleneck in hydrogen generation through electrolysis, particularly at large current operations. Thus, there is a huge interest in the development of highly active and robust non-noble metal based OER catalysts. Herein, we report excellent catalytic performance of oxygen vacancy enriched, nano-porous Mn_3O_4/Ni/$NiMnO_3$ architecture, synthesized *in situ* over NiMn substrate through high-rate straining and chemical dealloying. The multiphase active surface exhibits significantly low overpotentials of only 262 mV and 282 mV even at high current densities of 500 mA/cm^2 and 1000 mA/cm^2, respectively. Our first-principles analysis revealed the prevalence of multi-site lattice oxygen mediated pathways with two parallel mechanisms of direct evolution of O_2, (a) facile cleavage of Ni-O bonds at $NiMnO_3$ surface and release of lattice oxygen, (b) activation of under-coordinated Mn-O polyhedra at Ni/$NiMnO_3$ interface, and cleavage of OH group by protonation of surface O atoms. The presence of oxygen vacancy leads to electronic reconstruction, further enhancing the adsorption kinetics of reaction intermediates.

Introduction
Alarming environmental concerns combined with the rapid depletion of fossil fuels have triggered significant interest in alternative energy sources. Owing to its compelling properties as an energy carrier, hydrogen is considered an attractive alternative to fossil fuels. The generation of hydrogen via electrochemical water splitting is considered one of the most promising environmental-friendly, green technology[1-5]. The water-splitting process involves two independent reaction pathways that occur simultaneously: Hydrogen evolution reaction (HER:$2H^+ + 2e^- \rightarrow H_2$) and oxygen evolution reaction (OER:$2H_2O \rightarrow O_2 + 4e^- + 4H^+$). The oxygen evolution reaction, involving four electron transfer, is thermodynamically uphill process with sluggish kinetics, and poses a bigger challenge to the overall reaction kinetics[6-8] and large-scale functioning of fuel cells. Hence, there is a pressing need to develop high performance non-noble metal based electrocatalysts for OER.

In addition to structural stability and chemical selectivity, a crucial factor that determines the catalyst's performance for water splitting applications is its electronic structure, typically the partial occupancies of bonding and antibonding orbitals[9, 10], variable oxidation states[11] and tunable electrical conductivities[12]. In that context, the transition metal oxides (TMOs) are

1

considered promising electrocatalysts due to their special e_g orbitals and unique 3d electronic configuration[13]. Owing to its high affinity for OH⁻ adsorption and favourable electronic configuration of Ni^{3+} species $(t_{2g}^6 e_g^1)$[14], nickel has attracted a lot of attention for OER[15]. However, Ni^{3+} being an unstable oxidation state, nickel is typically alloyed with other transition elements such as Fe[16-20], Co[21, 22] or Mn[14, 23, 24]. These alloying additions enhance the overall catalyst performance along with its long-term stability. Moreover, the introduction of structural defects such as oxygen vacancies in the lattice structure has also been shown to improve the catalytic activity due to enhanced electrical conductivity and modulation of electronic structure[25]. Thus, creation of atomic scale defects in an appropriate alloy composition seems to be a promising pathway for developing high performance OER catalysts.

Despite the favourable electronic configuration of Mn^{3+} for OER $(t_{2g}^3 e_g^1)$, there are only a few studies on the role of Mn alloying addition in Ni[24, 26], particularly when Mn is in larger fraction (Mn$\geq$ 50%). The higher Mn fraction allows for creation of a porous microstructure, albeit with highly non-homogenous distribution[27]. In our previous work[28], we have developed a robust approach of integrating selective dealloying of Mn with high strain-rate deformation of NiMn alloy, resulting in *in situ* formation of nano-porous hierarchical architectures with a multi-phase structure. A simple two-step process involving short-burst of severe surface deformation and chemical dealloying is a quick and efficient technique for synthesizing binder-free, defect enriched, sturdy nano-porous microstructure with high chemical activity. Along with the unprecedented enhancement in specific capacitance and energy storage of these nano-structures, the high surface area of fine-grained nano-porous structures and surface hydrophilicity is quite promising to augment the reaction kinetics of water splitting reaction viz. OER. Herein, we investigate the catalytic activity of these deformation-induced oxygen-vacancy enriched nano-scaled NiMn oxides, and comprehensively evaluate their OER performance. We found that the oxygen abundant $Mn_3O_4/Ni/NiMnO_3$@NiMn heterostructures required overpotentials of only 262 mV and 282 mV even at high current densities of 500 mA/cm² and 1000 mA/cm², respectively, which is one of the best among most of the reported inexpensive OER catalysts. The *in situ* developed, robust nano-structures with high intrinsic activity demonstrate minimum degradation over time at large current operations. Our detailed theoretical analysis based on density functional theory (DFT) revealed distinct OER mechanisms and active sites on (001) Mn_3O_4, (100) $NiMnO_3$ phases and Ni/$NiMnO_3$ heterostructures. We propose that the higher catalytic activity of $Mn_3O_4/Ni/NiMnO_3$@NiMn heterostructures stems largely from the multi-site lattice oxygen-mediated (LOM) pathways for OER, with two co-operating mechanisms of direct O_2 evolution; cleavage of Ni-O bond and release of lattice oxygen at the $NiMnO_3$ surface, and activation of Mn-O bond at Ni/$NiMnO_3$ interface, with the cleavage of OH group to form O_2. The current work provides a new paradigm for designing efficient electrocatalysts for OER through surface activation, and investigating the mechanisms of multi-site OER activity, transcending the scalability constraints of OH/O/OOH adsorption.

Experimental details

Synthesis of nanoporous alloy: The pure elemental powders of 30 wt.% Ni and 70 wt.% Mn were mixed and then compressed using a hydraulic press to form small pellets. $Ni_{30}Mn_{70}$ alloy was synthesised via melting the pellets in an arc melter. The synthesized alloy was subjected to severe physical deformation to tailor the microstructure and introduce oxygen vacancies (OV). The physical deformation was performed using a 12 mm diameter tungsten carbide cylinder, which was rotated at 1800 rpm over the NiMn alloy surface. Thin strips of 100 μm thickness were cut

from the as-synthesized and physically deformed $Ni_{30}Mn_{70}$ alloy. Both the pristine and deformed samples were de-alloyed at 70 °C in 1 M $(NH_4)_2SO_4$ solution for 120 minutes and 90 minutes respectively.

Microstructural characterization: The microstructural analysis of as-synthesized pristine (NM_{PS}) $Ni_{30}Mn_{70}$ alloy; as-synthesized pristine dealloyed (NM_{DL}), physically deformed (NM_{OV}) and deformed dealloyed (NM_{OVD}) specimens was performed using field-emission scanning electron microscope equipped with energy dispersive spectroscopy (EDS), scanning transmission electron microscope (STEM), transmission electron microscope (TEM, FEI Titan 80–300) and atom probe tomography (APT). The cross-section samples for STEM and needle specimens for APT analysis were prepared using focussed ion-beam (FEI Helios NanoLab 660). The electron energy loss spectroscopy (EELS) maps and spectra were obtained using the Mn-L, Ni-L, and O-K edges at an energy dispersion of 0.25 eV/Ch using a Gatan 665 electron energy-loss image filter. Interactive Visualization and Analysis Software (IVAS), version 3.8.2 was used for the reconstruction and analysis of the APT data sets. The pore size distribution and surface area was determined through Brunauer-Emmett-Teller (BET) analysis, performed using Anton par Autosorb 6100 high vacuum gas sorption analyzer. The grain structure of NM_{PS} and NM_{OV} was analysed using Electron Backscatter Diffraction (EBSD). The crystal structure of all specimens was evaluated by using X-ray diffraction (XRD) measurement in a 2θ range of 30 to 80 degrees. The thin oxide layer on the dealloyed specimens i.e NM_{DL} and NM_{OVD} was analysed through X-ray photoelectron spectroscopy (XPS). XPS spectra of Ni, Mn, and O were recorded on the surface using a monochromatic Al-Kα X-ray source (1.486 keV, Scienta Omicron Nanotechnology).

Electrochemical testing: Electrochemical performance of NM_{PS}, NM_{DL}, NM_{OVD} and RuO_2 was evaluated in a three-electrode configuration using Biologic, VSP-3e potentiostat. The high purity graphite rod served as a counter electrode and saturated calomel electrode (SCE) as a reference electrode. A 1 M KOH (Sigma-Aldrich) solution was used as an electrolyte for carrying out all the electrochemical measurements. Before recording the data for linear sweep voltammetry (LSV), the experimental setup was stabilized by performing cyclic voltammetry for 50 cycles at 10 mV/sec scan rate in the range of 0.2 V~1 V vs SCE. The data for LSV were taken at 1 mV/s scan rate. All the LSV curves reported in the current study were corrected for the ohmic losses according to the equation: $E_{Corrected} = E_{Raw} − I*R_S$, where I is the current and R_S is the solution resistance which is obtained from the Nyquist plot of electrochemical impedance spectroscopy (EIS). All the potential values were converted to reversible hydrogen electrode (RHE) using the equation $E_{RHE} = E_{SCE} + 0.0592*pH + 0.242$. Chronopotentiometry was performed at different current densities in order to investigate the long term stability of electrodes. EIS measurements were obtained at 1.47 V vs RHE over a frequency range of 0.01 Hz to 100 kHz with a set AC voltage amplitude of 10 mV. The Echem analyst 7.03 was used to model the electrical equivalent circuit (EEC). To estimate the electrochemical double layer specific capacitance (C_{dl}), CVs were obtained at 1, 5, 10, 20, 40 mVsec^{-1} scan rates in a non-faradaic region.

Results and discussion
Microstructural characterization: The grain structures of as-synthesized pristine (NM_{PS}) and physically deformed (NM_{OV}) $Ni_{30}Mn_{70}$ alloy specimen is shown in Figure 1(a) and 1(b) respectively. The NM_{PS} sample showed a coarse grain structure with an average grain size of ~ 240±15 μm. The NM_{OV} sample showed more than an order of magnitude refinement in the grain
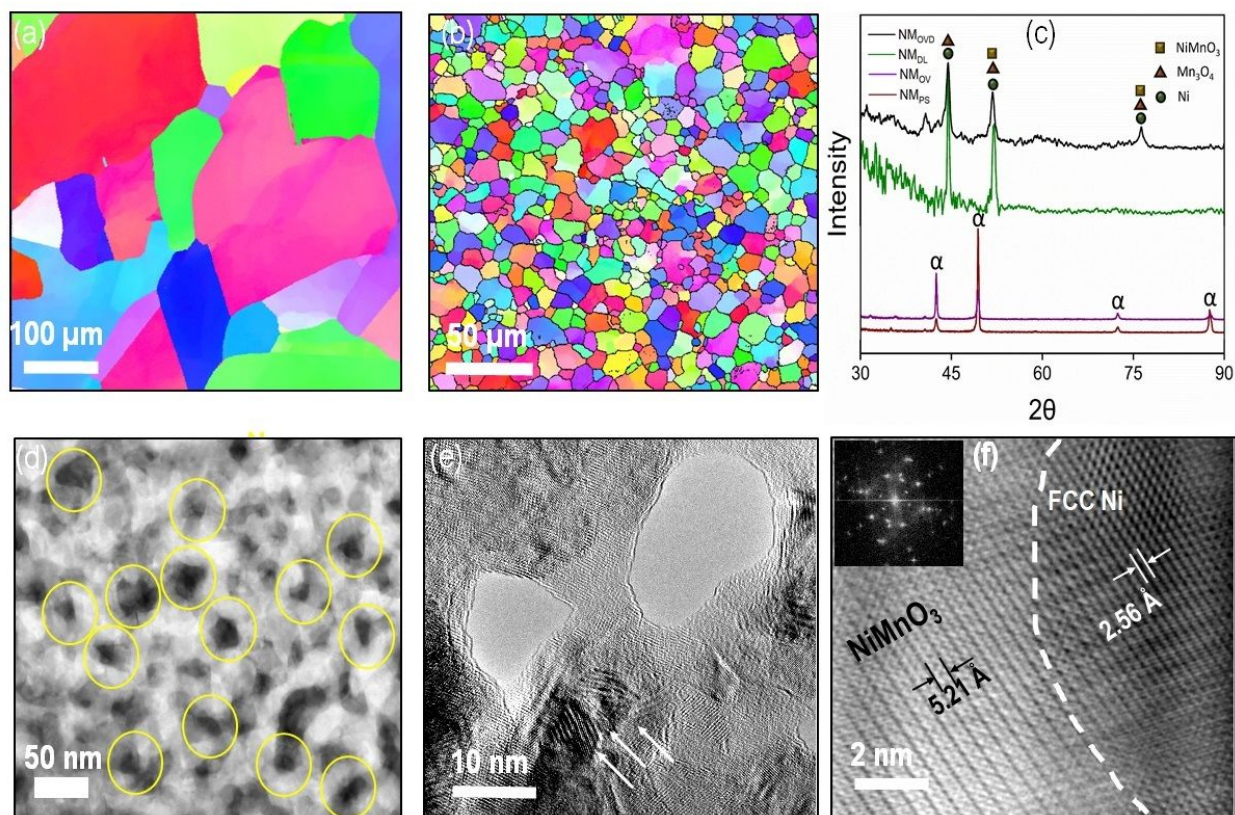
3

Figure 1: Electron Backscatter Diffraction (EBSD) images of (a) as-synthesized pristine (NM$_{PS}$), and (b) physically deformed (NM$_{OV}$) Ni$_{30}$Mn$_{70}$ alloy; (c) X-ray diffraction (XRD) analysis of NM$_{PS}$, NM$_{OV}$, as-synthesized pristine dealloyed (NM$_{DL}$), and deformed dealloyed (NM$_{OVD}$) specimen; High resolution transmission electron microscope (HR-TEM) images showing (d) uniform nano-porous structure, (e) fine nano-pores and the layered structure (f) well-resolved lattice fringes of the layered structure (NiMnO$_3$) and FCC Ni. α-phase in the XRD analysis represents Ni-Mn solid solution

size (~ 10±2 μm). The microstructure evolution in the as-synthesized pristine de-alloyed (NM$_{DL}$) and deformed de-alloyed (NM$_{OVD}$) specimens is shown in Figure S1(a) and S1(b). The NM$_{DL}$ shows sharp facets with cleavage-type morphology after dealloying (Figure S1(a)). In contrast, the NM$_{OVD}$ specimen showed a hierarchical architecture comprising micro-scale fine openings and nano-scale fibrous structure. The XRD analysis of NM$_{PS}$, NM$_{OV}$, NM$_{DL}$ and NM$_{OVD}$ is shown in Figure 1(c). Both NM$_{PS}$ and NM$_{OV}$ showed solid solution formation, α phase, without any signature of intermetallic phase formation. Further, NM$_{DL}$ and NM$_{OVD}$ present similar diffraction patterns that correspond to the oxides of nickel and manganese. Both NM$_{DL}$ and NM$_{OVD}$ samples showed NiMnO$_3$, and Mn$_3$O$_4$ as the primary oxides along with metallic nickel. The transmission electron image (TEM) images of NM$_{OVD}$ sample (Figure 1(d) and 1(e)) show a uniform distribution of fine pores with an average pore size of ~ 10 nm. The regions marked in Figure 1(e) also show a phase with a layered morphology. The high-resolution TEM image of the layered phase (Figure 1(f)) indicates well-resolved lattice fringes with interlayer spacing of 5.21 Å. Alongside, another phase with a lattice d-spacing of 2.56 Å, closely matching with inter-planar spacing of (011) Ni was also

seen. The pore size and surface area was determined using BET analysis (Figure S2). The pore size was found to vary between ~1 nm- 40 nm for both the specimens. However, the surface area of NM_{OVD} (13.56 m^2/g) was nearly an order of magnitude higher than NM_{DL} specimen (1.60 m^2/g).

To determine the phase chemistry, electron energy loss spectroscopy (EELS) and atom probe tomography (APT) were performed (Figure 2(a) and 2(b)) which confirmed the formation of oxides of Ni and Mn in NM_{OVD}. The EELS analysis and compositional portioning in APT also indicated a two-phase composite structure with Ni-rich region, completely devoid of manganese, and NiMn phase with the composition NiMnO$_3$ (Figure S3 and Figure 2(c)). The XPS survey spectra of NM_{DL} and NM_{OVD} were found to be similar (Figure S4). The high-resolution scans of Ni-2p, Mn-2p, O-1s for both the specimens are shown in Figure 3(a) – 3(f). The Ni 2p spectrum can be resolved into six distinct peaks for NM_{OVD} specimen. The peak situated at 854.43 (Ni^{2+}) and 855.92 eV (Ni^{3+}), along with its associated satellite peak at 861.45 eV, can be ascribed to Ni 2p3/2. In contrast, the two peaks, found at 872.27 eV (Ni^{2+}) and 874.20 eV (Ni^{3+}) along with its associated satellite peak at 874.20 eV correspond to Ni 2p1/2[29-31]. The Ni^{3+} peak may be attributed to Ni in NiMnO$_3$ phase [32]. The presence of oxygen vacancies in NiMnO$_3$ (refer to Mott-Schottky analysis below) results in lowering the oxidation state from Ni^{3+} to Ni^{2+}. The binding energies observed for Mn 2p3/2 at 640.48 eV and 642.43 eV correspond to Mn$_3$O$_4$ and Mn^{4+} oxidation states of Mn, respectively[33, 34], whereas 651.86 eV (Mn^{3+}) and 653.21 eV (Mn$_3$O$_4$) correspond to Mn 2p1/2[35, 36]. Furthermore, the 11.9 eV splitting width of both the broad peaks aligns with the presence of Mn$_3$O$_4$ [37]. Similar splitting width of two major peaks was observed for NM_{DL}, which corresponds to the presence of Mn$_3$O$_4$ in NM_{DL} specimen as well. The spectra for O 1s scan for NM_{OVD} specimen showed peaks at 529.6 eV and 531.3 eV that corresponding to lattice oxygen and oxygen vacancies respectively[38, 39], whereas NM_{DL} showed similar surface chemistry corresponding to peaks at 529.55 eV and 531.11 eV, respectively[40, 41]. However, Figure S4(b) highlights the difference in the oxygen vacancy peak, showing that the magnitude is higher in the NM_{OVD} specimen compared to the NM_{DL} specimen.

Oxygen evolution reaction (OER) performance: To maximize the OER performance, the dealloying time of NiMn$_{OVD}$ sample was first optimized as it significantly influences the electrochemical properties. By systematically varying the dealloying time from 30 minutes to 120 minutes, the optimal duration of dealloying was found to be 90 minutes for the NM_{OVD} sample. Figure S5 shows the *IR*-corrected linear sweep voltammetry curves (LSV) curves for different dealloying times. The charge carrier density (N_D) for NM_{DL} and NM_{OVD} was estimated using well-known Mott-Schottky analysis, expressed as: $N_D = [2/e_0\varepsilon\varepsilon_0]\left[d\left(1/C^2\right)/dV\right]^{-1}$, where, e_0 is electron charge, ε is the dielectric constant, ε_0 is the permittivity of the vacuum, C is the capacitance and V is the potential applied. Both specimens showed n-type semiconductor characteristics, indicated by the positive slope of Mott-Schottky plots (Figure 4(a)). The charge carrier density for NM_{OVD} was calculated to be nearly 4.5 times higher compared to NM_{DL} which is likely attributed to deformation-induced oxygen vacancies. The LSV curves for NM_{PS}, NM_{DL} and NM_{OVD} are shown in Figure 4(b). The data for RuO$_2$ is also given for comparison. The overpotential required to deliver different current densities was obtained from the LSV curve and is shown in Figure 4(c). It is evident that NM_{OVD} showed the lowest overpotential values at all current densities amongst all specimens. Even at large current densities of 500, and 1000 mA cm$_{geometric}^{-2}$, the overpotential values were only 262, and 282 mV respectively, which are amongst the best reported in the literature (Table S1). The LSV data was employed to obtain the Tafel slope for various specimens, as illustrated in Figure 4(d). Notably, NM_{OVD} specimen exhibited a low
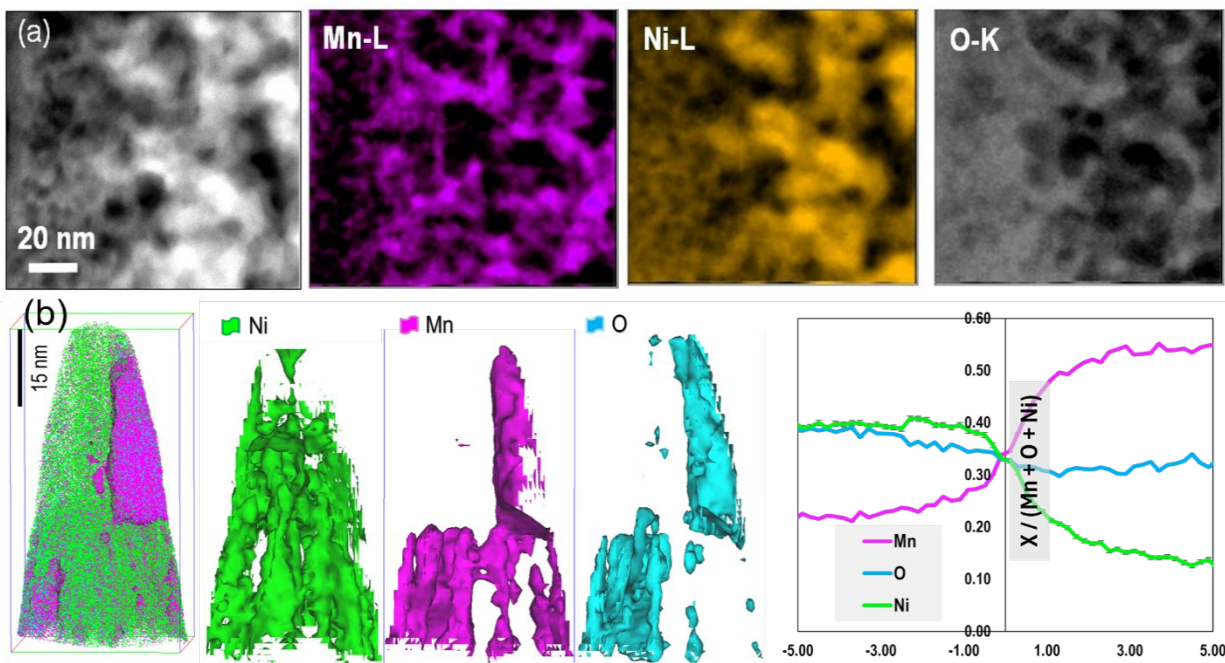
5

Figure 2: (a) Electron energy loss spectroscopy (EELS) mapping of Mn-L edge, Ni-L edge and O K-edge for NM_{OVD}; Atom probe tomography (APT) results of the needle specimen from NM_{OVD} showing (from left to right) all ions overlayed with iso-surfaces, Ni iso-surface encircling regions with >25 at. % Ni; Mn iso-surface encircling regions with >25 at. % Mn; O iso-surface encircling regions with >25 at. % O, (c) proximity histogram across the interface of Ni-rich side and $NiMnO_3$ structure.

Tafel slope of 34.61 mV dec^{-1}, in contrast to the RuO_2 catalyst (67.62 mV dec^{-1}), NM_{DL} (71.68 mV dec^{-1}) and NM_{PS} (78.12 mV dec^{-1}) respectively. The lower Tafel slope for NM_{OVD} indicates its faster charge transport kinetics.

Further, to probe the intrinsic activity of NM_{DL} and NM_{OVD} specimens, the double layer capacitance (C_{dl}) was determined from cyclic voltammetry response in the non-faradaic region (Figure S6). The C_{dl} for NM_{OVD} (79.26 mF/cm^2) was found to be higher compared to NM_{DL} (39.06 mF/cm^2) (Figure S6(c)). Using the ratio C_{dl}/C_s, where, C_s denote the specific capacitance (~40 µF/cm^2), the electrochemical active surface area (ECSA) was calculated to be 1981cm^2 and 976.5 cm^2 for NM_{OVD} and NM_{DL} respectively. The ECSA normalized LSV curves (Figure S6(d)) indicate that NM_{OVD} requires only 335 mV to reach current density of 0.2 mA/cm^2 compared to 620 mV for NM_{DL} to reach similar current density. Thus, the superior catalytic performance of NM_{OVD} is attributed to its larger active surface area as well as increased intrinsic activity, emerging from the surface activation on physical deformation. The durability of both NM_{DL} and NM_{OVD} for OER was assessed using chronopotentiometry, as shown in Figure 4(e). During the 24-hour test period, there was only a marginal increase in the potential even at high current density of 500 mA cm^{-2}, demonstrating high stability of NM_{OVD}. In contrast, NM_{DL} and RuO_2 exhibited a significant increase in the potential required to sustain the same current densities. The surface composition post-OER testing was obtained using XPS analysis (Figure S7) which showed minimal change in the surface chemistry. The Ni 2p3/2 and Ni 2p1/2 peaks, which are centered at 855.6 eV and 873.4

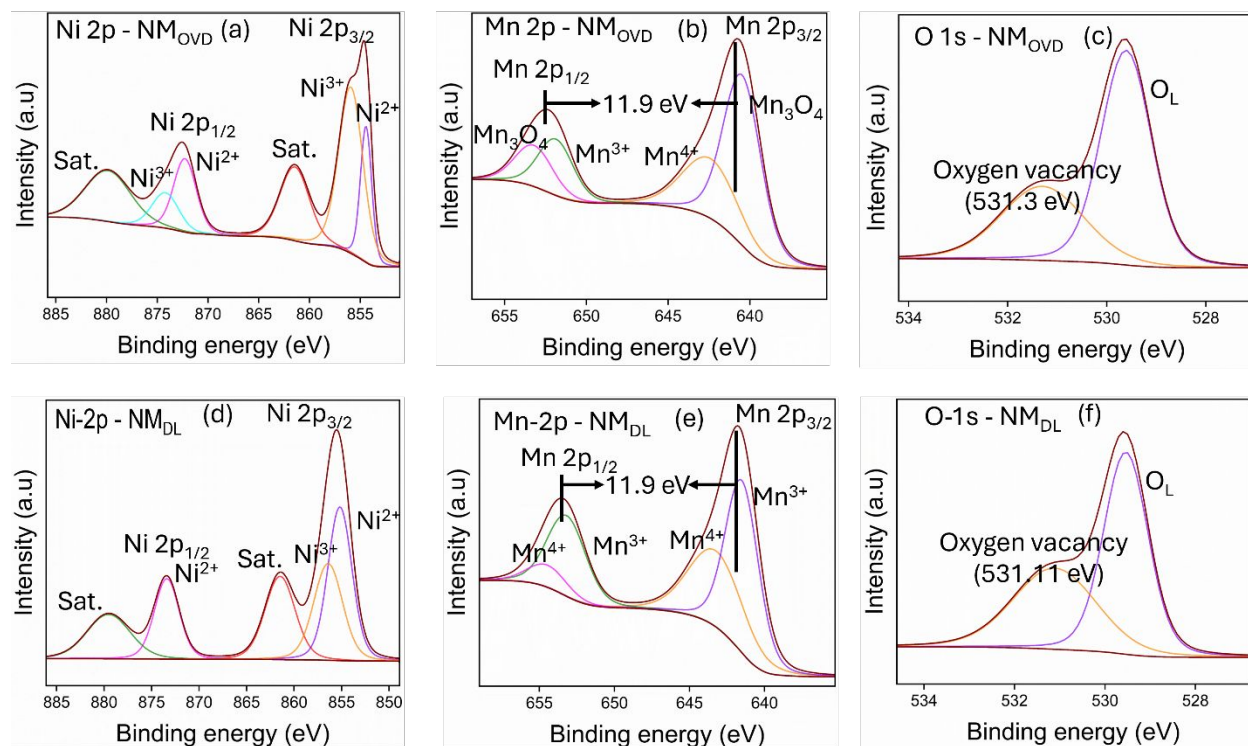**Figure 3**: X-ray photoelectron spectroscopy (XPS) high resolution spectra for (a) to (c) NM$_{DL}$ - Ni2p, Mn2p and O1s, (d) to (f) NM$_{OVD}$ - Ni2p, Mn2p and O1s.

eV, respectively, can be attributed to Ni^{2+} whereas Mn exists in Mn$_3$O$_4$ state, maintaining the splitting width of both the broad peaks to 11.9 eV[37, 42]. However, the peaks at 641.20 eV and 643.50 eV correspond to Mn^{3+} and Mn^{4+} respectively, in Mn 2p3/2[43, 44], whereas the peaks at 652.86 eV and 654.71 eV correspond to similar oxidation states of Mn in Mn 2p1/2[45, 46]. The sub-peaks in O1s with binding energies at 529.55 eV and 530.90 eV are identified as the reflections of lattice oxygen (O$_L$) and oxygen vacancies respectively[47]. The O1s peak representing oxygen vacancies got further intensified (inset Figure S7(d)) after OER testing as a consequence of cleavage of Ni-O bond (discussed in theoretical analysis). The polarization resistance of all the specimens was determined using electrochemical impedance spectroscopy (EIS). Figure 4(f) shows the Nyquist plot for NM$_{OVD}$, NM$_{DL}$ and RuO$_2$. The equivalent electrical circuit (EEC) used for fitting the experimental data is shown in the inset of Figure 4(f). R_{PI} and C_{PEI} are the electrical components representing polarization resistance and the constant phase element at the oxide and electrolyte interface, while R_s represents the solution resistance. NM$_{OVD}$ shows the least polarization resistance (2.6 Ω) compared to NM$_{DL}$ (7.5 Ω), and RuO$_2$ (3.3 Ω) respectively, indicating better charge transport in NM$_{OVD}$. The solution resistance in all cases was found to be similar (3.5 Ω). Structural evolution during OER has been reported to play a key role in explaining the excellent catalytic activity[48-50]. Using operando X-ray absorption spectroscopy, the correlation between structural evolution of Fe-Ni (oxy)hydroxide catalysts and their OER performance was investigated[48]. The changes in the valence state, coordination environment, and structural disorder of catalysts at different applied potentials were obtained. The results indicate structure transformation from the pre-catalyst to the (oxy)hydroxide at the catalytic region which was
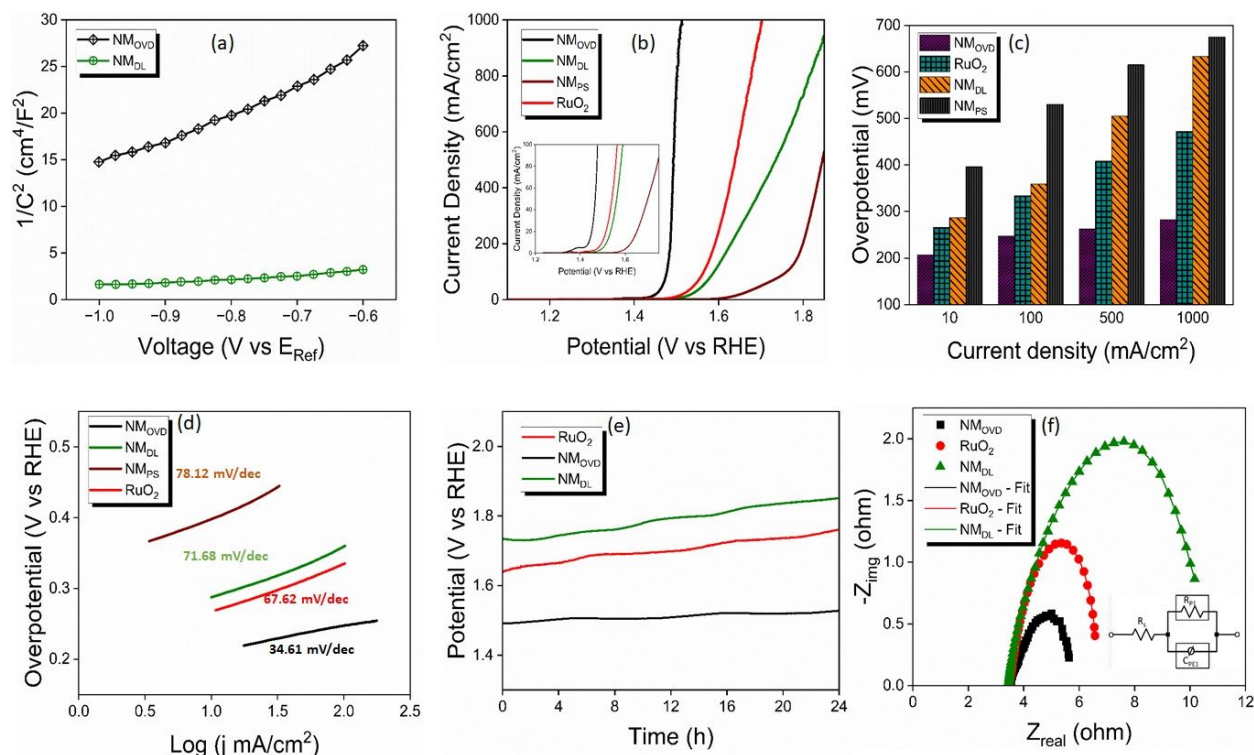
Figure 4: (a) Mott-Schottky plots for NM_{DL} and NM_{OVD}; (b) Linear sweep voltammetry (LSV) curves for NM_{DL}, NM_{OVD}, NM_{PS} and RuO_2, (c) comparison of overpotential values at different current densities, (d) Tafel slopes for NM_{DL}, NM_{OVD}, NM_{PS} and RuO_2, (e) chronopotentiometry curves at 500 mA cm^{-2} for 24 hours, and (f) Nyquist plots for NM_{DL}, NM_{OVD}, NM_{PS} and RuO_2

identified as the active phase for the OER. With increase in disordering factor at higher applied potentials, the NiO bond length tends to become elongated and thereby weak, making it easier for oxygen species to react and evolve during the OER. The study demonstrates that the origin of enhanced OER activity of in situ-generated metal (oxy)hydroxides is increased structural disorder and dynamic structural evolution during OER. Similarly, the local coordination structure distortion and disordering of the active sites were proposed to be responsible for the greatly enhanced OER performance of bimetallic Ni–Fe selenide[49]. The structural evolution during OER resulted in the transformation from selenides to (oxy)hydroxides. The in situ generated distorted structure with a high disorder degree was inherited from the heteroatom-containing structure in the pre-catalysts. In another study[50], it was found that the disordered birnessite layer (δ-MnO$_2$) produced through anodic conditioning from voltage cycling was significantly more active toward OER than the original birnessite phase.

Theoretical Analysis: We now understand the reaction pathways and catalytic activity of multi-step OER over the complex multiphase nano-structures using density functional theory (DFT)-based theoretical analysis. In the alkaline condition, the hydroxyl group (^-OH) oxidizes at the electrocatalyst (anode) to form H_2O and O_2, with the release of electrons. At standard

conditions (T = 298.15 K, p_{H2} = 1 bar), the free energies of adsorption of the reaction intermediates in alkaline medium, are calculated as[51]:

$$\Delta G_1 = G_{*OH} - G_* + \frac{1}{2}\mu^o{}_{H_{2(g)}} - \mu^o{}_{H_2O(l)} - 0.0597\, pH \qquad (1)$$

$$\Delta G_2 = G_{*O} - G_{*OH} + \frac{1}{2}\mu^o{}_{H_{2(g)}} - 0.0597\, pH \qquad (2)$$

$$\Delta G_3 = G_{*OOH} - G_{*O*} + \frac{1}{2}\mu^o{}_{H_{2(g)}} - \mu^o{}_{H_2O(l)} - 0.0597\, pH \qquad (3)$$

where, G_* is the total energy of the clean surface, G_{*OH}, G_{*O} and G_{*OOH} are the free energies of surfaces with adsorbed intermediates; *OH, *O and *OOH, respectively. The free-energy terms include the corresponding vibrational zero-point energy and entropy of the adsorbed species. $\mu^o{}_{H_2}$, $\mu^o{}_{O_2}$ and $\mu^o{}_{H_2O}$ are the free energies of the hydrogen gas, oxygen gas and liquid water in standard conditions. Here, the voltage U = 0 V, and the free energies of reaction intermediates calculated using DFT are referenced with computational Hydrogen electrode (CHE)[52], at the pH value of 14. The relative adsorption energies of these intermediates are crucial parameters for determining the potential-limiting step (PLS) of the overall OER.

Our detailed microstructural analysis of the synthesized nano-structured architectures shows that two distinct phases stabilize on selective dealloying and physical deformation of NiMn alloy, (a) Mn_3O_4 phase, and (b) $NiMnO_3$ oxide in the Ni matrix within the nano-flakes formed in NM_{DL} and NM_{OVD}. Hence, we analyze the surface activities of Mn_3O_4 and $NiMnO_3$ phases in their pristine forms, and further study the effect of defects; O-vacancies in $NiMnO_3$ and Ni/ $NiMnO_3$ interface on the overall catalytic performance of the activated surface. The structures of Mn_3O_4 and $NiMnO_3$ are highly anisotropic. Hence, we first determined the energetically feasible surface terminations in these oxide phases, considering the surface energies and atomic structural changes on/near the surface on structural optimization. The adsorption behavior of reaction intermediates on each of the relaxed surfaces was studied by first determining the inequivalent sites for OH adsorption, taking into account the chemical environment around the adsorbate and the symmetry of the substrate. The resulting structures were optimized until the force on each atom was less than 0.02 eV/atom.

Typically, in most computational studies on the thermodynamics of electrochemical reactions, the electrocatalyst performance is dictated by the overpotential associated with the overall OER reaction[53]. This paradigm is generally applicable to single-site reactions. However, in multi-site reactions, the sequence of intermediate steps and the associated energies become important in understanding the alternate pathways of a reaction [54]. Here, we assessed the relative stabilities of the intermediates in a sequential way to determine the catalytic activities and their preferred sites on the electrode for OER, without restricting the analysis to the scaling relationships between binding energies of *OH, *O and *OOH relevant in the single-site OER. We identified the active sites, adsorption energies, and hence the PLS, and reaction mechanism (single- or multi-site) of OER in each phase. In this study, we have not included the solvent effects since the dielectric constants of the nano-structured phases containing defects, and complex interfaces cannot be determined precisely. Further, in the presence of KOH ions we expected the formation of Ni-based hydroxides on the surface as the reaction proceeded. However, the non-declining catalytic activity of the $Mn_3O_4/NiMnO_3$@NiMn heterostructures, significantly higher than that of Ni-hydroxides [55-57], suggests the prevalence of stable Ni and Mn- based oxides as the catalytically active phases.

Mn₃O₄ phase: In Mn_3O_4, the (001) step surface consisting of both Mn^{2+} and Mn^{3+} species (Figure 5(a)), with the latter containing cleaved Mn-O bonds, forms the suitable surface for adsorption with its lowest cohesive energy $E_{cohesive}$ = -2.35 eV per formula unit. As reported by Liu et. al.[58], this surface is preferentially active, in comparison to the (101) surface. Typically, Mn_3O_4 exhibits superior catalytic activity towards OER, when doped with metallic elements[59], or when synthesized as nanoparticles[60], or atomically thin 2D-form[61]. In our experiments, since Mn_3O_4 formed the nano-flakes with a thickness of nearly 30-50 nm, we analysed the catalytic activity of Mn_3O_4 slab at the (001) surface (Figure 5(a)). The OH adsorption on the (001) surface of Mn_3O_4 occurred at three energetically feasible sites, (i) over the Mn^{3+} truncated octahedron (ΔG_1 = -2.32 eV/ion) (Figure 5(b)), (ii) on the bridging O between two Mn^{3+} ions, (ΔG_1 = -2.09 eV/ion) (Figure 5(c)), and (iii) over the Mn^{2+} tetrahedron, which shifts to the surface and occupies the octahedral void (ΔG_1 = -2.00 eV/ion) (Figure 5(d)) on structural optimization, at equilibrium potential U = 1.23 V with respect to SHE. Deprotonation of the adsorbed OH is highly endothermic on the site (i) with an overpotential of 1.84 eV/ion, but is energetically favourable for sites (ii) and (iii) involving -1.49 and -1.52 eV/ion. Further, *OOH formation at site (ii) is thermodynamically favoured with ΔG_3 = -1.58 eV/ion (Figure 5(e)), while O_2 evolution is the PLS of OER with DG = 2.8 eV. The latter agrees with the reported [61]OER activity of (112) surface of the ultrathin Mn_3O_4 wherein the O_2 formation from *OOH is energetically uphill, along with *OOH formation from O*, albeit with lower over-potential values than on (001) surface. To discern the kinetics of O* → *OOH step (marked as arrow in Figure 5(e)), we determined the energy of transition state for this elementary step using nudged elastic band (NEB) method[62]. The activation barrier for *OOH formation is 0.76 eV. To further explore the possibility of facile *OOH formation involving multiple surface sites, that is, in high coverage regime, we added OH groups in the neighbourhood of *O sites. We found that both Mn^{3+} and Mn^{2+} ions are the sites suitable for *O and *OH, with the formation of H_2O (Figure 5(f)). However, there is no indication of the bonding of *O and surrounding OH ions to form the *OOH group. This suggests that Mn_3O_4 (001) surface in its native form is not very efficient for the overall OER reaction, one, due to lower selectivity of *OH and *O reaction intermediates, and two, because of the infeasibility of *OOH formation.

NiMnO₃ phase: $NiMnO_3$ is a semi-conducting material with a band gap of ~2 eV (Figure S8), and prevalence of Mn-3d and O-2p states close to the Fermi-level. The (001) surface of $NiMnO_3$ forms a coherent interface with closed-packed (111) surface of Ni with small lattice strains (1.4 %)[28]. Hence, we analyzed the exposed (110) surface of $NiMnO_3$ for its catalytic activity (Figure 6(a) and 6(b)). All chemical species viz. Mn-, Ni- and O- are exposed on this surface which further allows us to understand the cooperative effect of both the transition elements on the chemical activity of $NiMnO_3$ towards OER. The electronic structure of the (110) surface shows a half-metallic nature with O-2p states in the band-gap region, and an overall decrease in band gap from 2.0 eV in bulk phase to 1.0 eV at the surface (Figure 6(c)), indicating enhanced electronic conduction due to O-2p states. On OH adsorption at distinct surface sites, we found that the most favorable configuration on the (110) $NiMnO_3$ shows the direct formation of O_L-O group through breaking of Ni-O_L (here O_L refers to lattice O) bond (Figure 6(d)), as seen in the change in Ni-O distance from 1.78 to 2.62 Å, while the neighbouring O_L bridged between Mn- and Ni- accepts the proton (ΔG_1 = -2.64 eV at U = 0 eV with respect to SHE)[63]. The calculated transition state energy of this multi-site adsorption-evolution step is 1.78 eV, which stems from the cleavage of Ni-O_L and O-H bond. The dangling O_L atom transfers $\sim$ 0.3 a.u. charge to Ni and forms O_L-O bond, resulting in an oxygen vacancy. The atypical charge transfer from electronegative O to Ni atom can be understood from the electronic density of states of $NiMnO_3$ surface (Figure
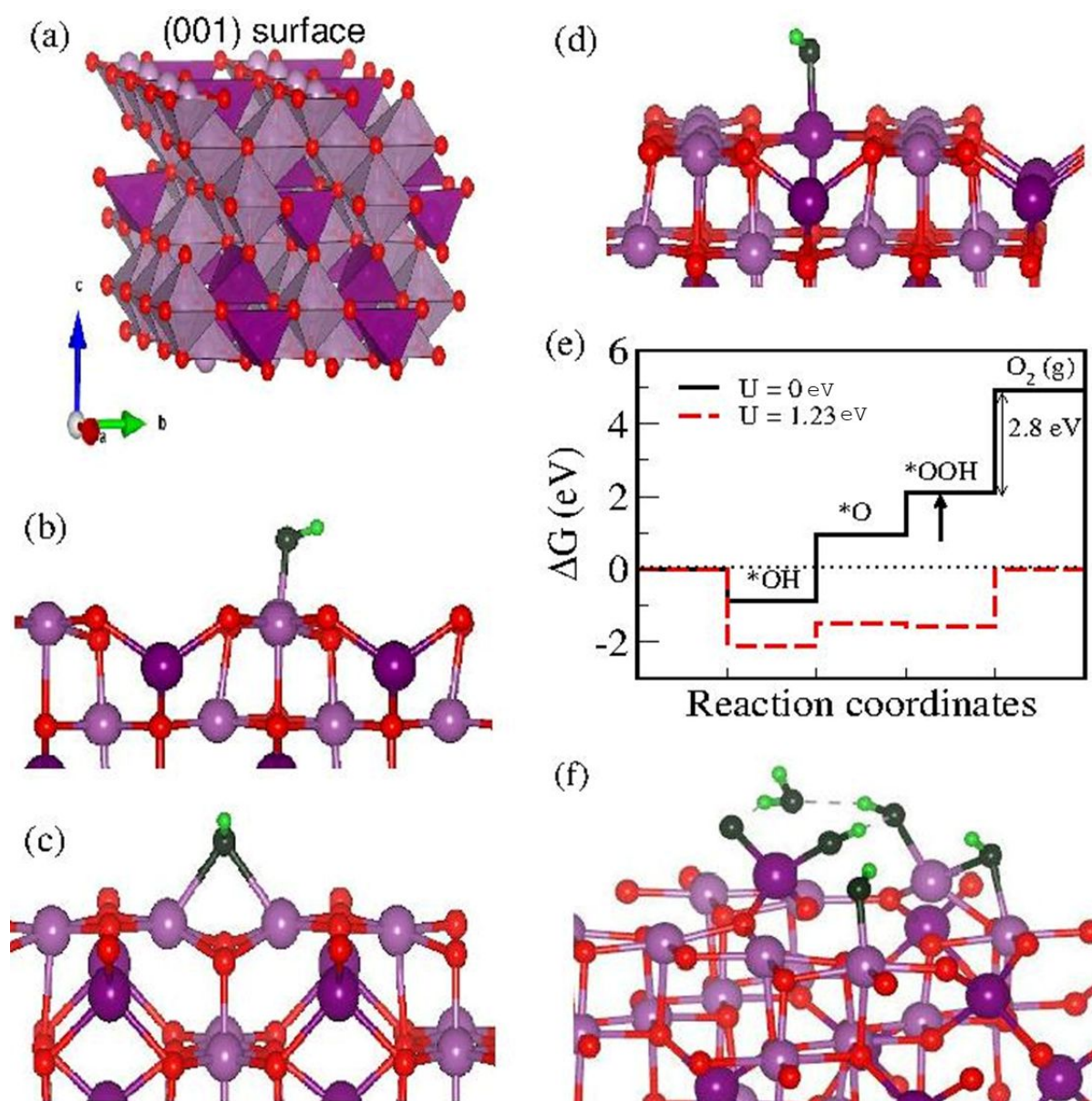
Figure 5: **OER activity on (001) Mn₃O₄**. (a) atomic structure of (001) Mn_3O_4 showing alternating octahedral Mn^{3+} and tetrahedral Mn^{2+} polyhedra, shown in light purple and magenta respectively, along the c-axis, (b-d) favorable adsorption sites for *OH with ΔG_{*OH} = -2.32, -2.09 and -2.00 eV/ion, respectively. The O and H of the adsorbate are shown in dark and light green respectively, to distinguish from the lattice O atom (shown in red), (e) adsorption energies of reaction intermediates at single Mn^{3+} site, showing energetically uphill O_2 evolution, (f) prevalence of *OH and *O on Mn_3O_4 surface when neighbouring OH interact with *OH, disfavouring *OOH and O_2 formation.
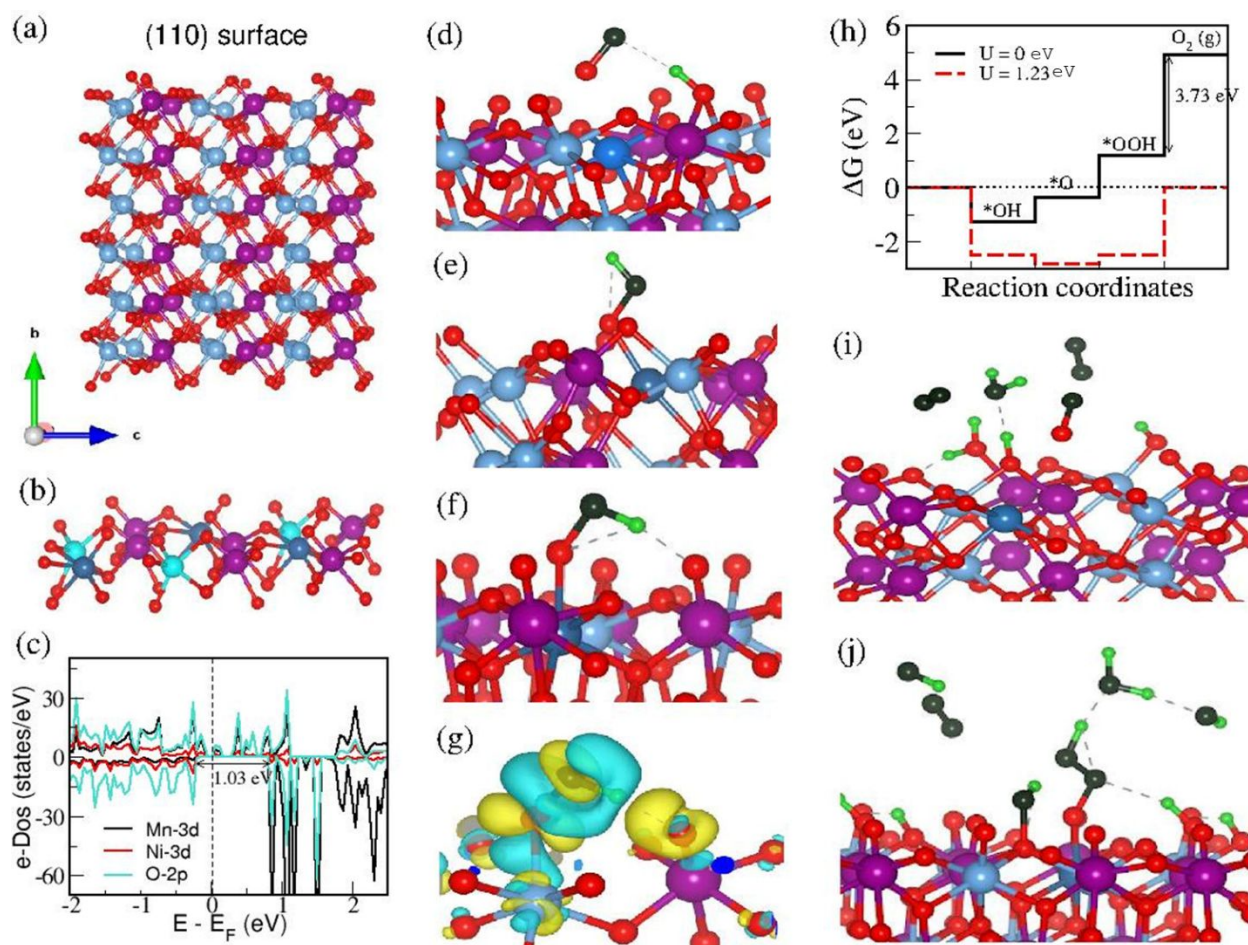
Figure 6: **OER mechanisms on NiMnO₃ surface**. (a) (110) surface of NiMnO₃, showing the occurrence of both Mn- and Ni- atomic species, Ni: light blue, Mn: magenta, O: red, (b) symmetry-inequivalent Ni sites, with distinct coordination with surface O atoms, Ni with dangling O (dark blue), and Ni forming Ni-Mn-Ni bridged O (in cyan), (c) electronic density of states of NiMnO₃ slab showing surface Mn-3d and O-2p in the band-gap region, (d) OH adsorption showing breaking of Ni-O$_L$ bond, suggesting the plausibility of LOM mechanism, (e-f) OH adsorption at Ni-O site and nature of charge transfer, (g), showing higher charge density (yellow color) over the neighbouring O atom of Mn-O bond, (h) free energies of reaction intermediates for single-site OER showing high overpotential for *OOH formation and O₂ evolution in NiMnO₃, (i-j) preferred LOM mechanism, assisted by cleavage of Ni-O$_L$ bond (i), and charge transfer between adsorbate and surface (j), for direct O₂ evolution.

6(c)), wherein the Ni-3d states have lower energy levels than O-2p valence states[64]. Further, the e-DoS of distinct O atoms bonded to the Ni atoms (as marked in dark blue color in Figure 6(b)) are starkly different, with dangling O atoms showing high density of O-2p states and absence of an energy gap (Figure S9 (a)), while the bridging O atoms show a gap of ~1 eV (Figure S9 (b)). This indicates a possibility of facile electron transfer from dangling O to surface Ni atoms, resulting in enhanced covalent character of the Ni-O bond[64]. Deprotonation of the surface (*O-O$_I$ + O$_{II}$-H + OH- → *O-O$_I$ + O$_{II}$ + H₂O) is

thermodynamically favorable with DG_2 = -1.6 eV/ion, with a small activation barrier of 0.37 eV, corresponding to an intermediate configuration with -H--O- hydrogen bonds (Figure S10).

　　　Two other surface sites show energetically favorable OH adsorption on $NiMnO_3$ surface (ΔG_1 = -1.38 eV/ion and -1.25 eV/ion) (Figure 6 (e-f)). Here, the OH group attaches to Ni-O dangling bond, with different orientations of *O-H in two configurations, elongating the Ni-O bond from 1.70 to ~2.03 Å. The electronic charge density in the latter shows negative charge on O bonded to Mn, favouring O_L-H formation, and depletion of charge over Ni-O_L bond, indicating possible cleavage of Ni-O_L bond, with O_2 evolution (Figures 6(g)). The deprotonation step is thermodynamically quite favorable (ΔG_2 = -0.50 eV and -0.39 eV respectively) with respect to SHE at pH = 14, resulting in two distinct configurations: Ni-O_L-O formation in the former, while the bridging O between Mn- and Ni in the latter. The Mn-O-Ni site is not suitable for the *OOH formation. The single-site *OOH formation over the Ni-O_L-O group is energetically uphill with DG_3 = 1.18 eV/ion, and ΔG = 3.73 eV for O_2 evolution, disfavouring AEM pathway for OER. As shown by Grimaud et al[65], the OER activity as well as the reaction mechanism is governed by the metal-oxygen covalency governs. These authors showed that the oxidation of lattice oxygen during OER can enhance the O_2 evolution. Further, the OER activity on the oxygen site is activated when the electronic states near the fermi level attains substantial O 2p character, resulting in greater covalency of the metal-oxygen bond. Such material systems also demonstrate pH dependent OER kinetics. In the current study, the theoretical analysis shows high density of O-2p states in $NiMnO_3$ phase, resulting in charge transfer from O_L atoms to Ni, along with the direct formation of O_L-O group through breaking of Ni-O_L bond. Thus, the high covalency of Ni-O_L bond suggest the prevalence of LOM mechanism, which is also supported by the pH dependence of the OER activity of the current material system (Figure S11).

Defects and OER mechanism: We now discuss the effect of defects viz. O vacancies and Ni/$NiMnO_3$ interface on the catalytic activity of the Mn_3O_4/$NiMnO_3$@NiMn heterostructures. The formation of O-vacancy in $NiMnO_3$(110) surface is highly dependent on the symmetry and coordination environment of different O sites on the surface. Considering two sites, (i) the dangling O_L of the Ni-O bond, and (ii) the O_L at the intersection of Ni-Ni-Mn octahedra, we optimized the structures containing these O vacancies (Figures 7(a) and 7(b) respectively). The formation energies, E_{vac} = -2.48 eV/vacancy and -0.75 eV/vacancy, respectively indicate that O-vacancies are energetically feasible in $NiMnO_3$, albeit with significant difference in E_{vac}. Energetically feasible O vacancies corroborate the existence of Ni in Ni^{2+} states (in O-vacancy enriched $NiMnO_3$), obtained from the XPS analysis. Structural optimization shows octahedral distortion in (i), and structural reconstruction in (ii) with formation of triangular prismatic and square pyramidal Ni-O polyhedral at the surface (Figure 7(b)). The electronic structure of the latter surface shows a sharp increase in Mn-3d and O-2p states at the conduction band minimum (CBM) (Figure S12) signifying enhanced oxidation kinetics. The adsorption of *OH and *O intermediates over the vacancy site (i) is unfavorable with ΔG_1 ~ 0.80 eV/ion, and ΔG_2 ~ 1.35 eV/ion with respect to SHE. This is primarily due to the optimal charge density over Ni of cleaved Ni-O group, and enhanced stability of the structure containing O-vacancy. The reconstructed structural units around vacancy site (ii) catalyze the OER due to very low single-site OH adsorption energy ΔG_1 = -2.50 eV (Figure 7(c)), with a very small activation barrier of 0.25 eV. The deprotonation step is favorable with ΔG_2 = -2.2 eV/ion, albeit with a higher activation barrier for *OH → *O step of 1.32 eV (see Figure S13 for the transition state). This
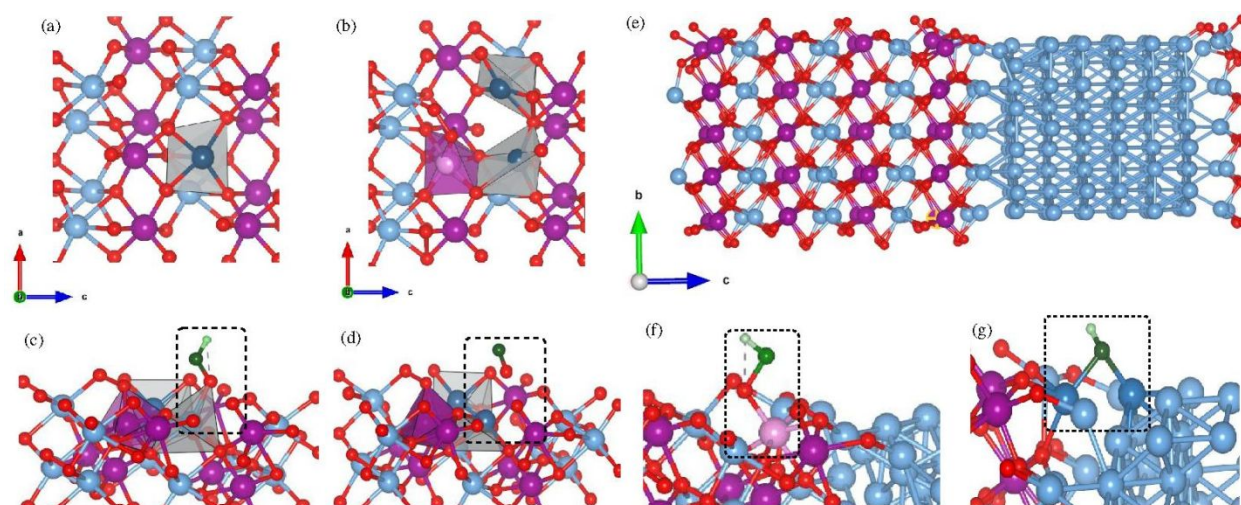
13

Figure 7: **Effects of O vacancies and Ni/NiMnO$_3$ interface on OER activity**. Left Panel: (a) vacancy configuration with very low formation energy, (b) favourable vacancy configuration for OER activity showing Ni-O trigonal prismatic, square pyramidal polyhedral and distorted Mn-O octahedra, viewed along [110] direction (c-d) active site for *OH adsorption and deprotonation, with feasible LOM mechanism. Right Panel: (e) Ni/NiMnO$_3$ heterostructures along [001] direction of NiMnO$_3$ and surface along [110], (f-g) active sites for OH adsorption close to the interface; O atom of under-coordinated Mn-O octahedra (f), and Ni-Ni bridge configuration (g).

involves elongation of Ni-O$_L$ bond from 1.92 to 2.06 Å, and is the energy required to activate the LOM mechanism[66] in NiMnO$_3$ containing O-vacancy (Figure 7(d)).

Lastly, Ni/NiMnO$_3$ interface (Figure 7(e)) has a marked effect on the OER activity of the nano-structured architecture. The adsorption of OH ions at distinct sites close to the interface results in two energetically favorable sites: (i) the Mn-O site, $\Delta G_1 \sim$ -1.20 eV, and (ii) O-H ion bridged across Ni-Ni, $\Delta G_1 \sim$ -3.75 eV (Figure 7(f) and (g)). The former site is the under-coordinated Mn present at the interface, which exhibits a sharp increase in the density of states at the Fermi level and at CBM (Figure S14), signifying its role in the oxidation of *OH. Hence, the presence of Ni/NiMnO$_3$ interface results in the activation of an additional Mn-O adsorption site, which is energetically infeasible on the pristine NiMnO$_3$ surface $\Delta G_1 \sim$ 0.82 eV. Deprotonation of the *OH on Mn-O is also favorable ($\Delta G_2 \sim$ -0.54 eV). Further, the interaction of the O* with neighboring OH ions at the surface shows the direct formation of O$_2$ and H$_2$O molecules (Figure S14). Since the O$_2$ formation does not involve cleavage of M-O (M: Ni or Mn) bond, the Ni/NiMnO$_3$ interface favors electro- mediated O$_2$ evolution at the surface. Here, highly electronegative surface O assists in cleavage of O-H bonds of the adsorbate, by bonding with H ions. This alternate electronic-transfer driven mechanism is another LOM pathway of OER in the nano-structured NiMn oxides, reminiscent to the mechanisms observed in Ni hydroxides[67].

14

Conclusions

In summary, we demonstrate a new synthesis pathway involving severe surface deformation and chemical dealloying of NiMn-alloy, that results in binder-free *in situ* formation of O-vacancy enriched, nano-porous Mn_3O_4/Ni/$NiMnO_3$@NiMn heterostructures over the NiMn substrate. The unique multiphase nanoarchitecture is highly efficient toward oxygen evolution reaction in alkaline media even at large current densities. The catalytic performance is one of the best among most of the reported inexpensive OER catalysts and are significantly better compared to state-of-the art RuO_2 catalysts. The multi-site adsorption mechanisms of OER reaction intermediates on different synthesized phases are theoretically analysed. The (001) surface of Mn_3O_4 shows high activation barrier for *O/*OOH and *OOH/O_2 formation, limiting its catalytic activity. The (110) surface of $NiMnO_3$ favours multi-site lattice-oxygen mediated mechanism of OER, with an activation energy of 1.78 eV on the pristine surface, and 1.32 eV on the O-vacancy containing surface, highlighting the role of O vacancies in the OER activity of the synthesized heterostructures. The pH dependence of OER activity supports the lattice-oxygen oxidation and presence of LOM mechanism for OER. The mechanism involves the cleavage of Ni-O bonds, which stems from facile transfer of electronic charge from dangling O to Ni atoms, giving rise to energetically favourable direct O_2 evolution. This mechanism is self-propagating, self-repairing and reversible which proceeds by breaking/reforming of Ni-O bonds. Further, the presence of Ni/$NiMnO_3$ interface results in an additional active site involving the under-coordinated Mn at the interface, which is absent on the pristine $NiMnO_3$ surface. The activation of Mn-O site results in a yet another mechanism of electron-mediated O_2 formation, from the cleavage of O-H bonds, by protonation of surface O atoms. Thus, our work provides a new approach for designing efficient electrocatalysts for OER through surface activation of NiMn oxides, and investigating the mechanisms of multi-site OER activity.

Competing interests: The authors declare no competing interests.

Data Availability: Data are available upon request from the authors

Author contributions

AT: Investigation, Formal Analysis, writing– original draft; **AK**: Investigation, Formal Analysis; **RKS:** Data curation, writing – review & editing; **EB:** Investigation, Formal Analysis, writing – review & editing; **BG**: Investigation, Formal Analysis, writing – review & editing; **MB**: Formal Analysis, writing– original draft, writing – review & editing; **HSA**: Conceptualization, Methodology, Supervision, Resources, Writing – review & editing.

References

1. A.-L. Wang, H. Xu and G.-R. Li, *ACS Energy Letters*, 2016, **1**, 445-453.
2. X. Gao, H. Zhang, Q. Li, X. Yu, Z. Hong, X. Zhang, C. Liang and Z. Lin, *Angewandte Chemie International Edition*, 2016, **55**, 6290-6294.
3. X. Zhang, H. Yi, M. Jin, Q. Lian, Y. Huang, Z. Ai, R. Huang, Z. Zuo, C. Tang and A. Amini, *Small*, 2022, **18**, 2203710.
4. A. Sivanantham, P. Ganesan and S. Shanmugam, *Advanced Functional Materials*, 2016, **26**, 4661-4672.
5. Y. Sun, Z. Xue, Q. Liu, Y. Jia, Y. Li, K. Liu, Y. Lin, M. Liu, G. Li and C.-Y. Su, *Nature communications*, 2021, **12**, 1369.
6. X. Fan, S. Tan, J. Yang, Y. Liu, W. Bian, F. Liao, H. Lin and Y. Li, *ACS Energy Letters*, 2021, **7**, 343-348.
7. Y. Yang, Y. Kang, H. Zhao, X. Dai, M. Cui, X. Luan, X. Zhang, F. Nie, Z. Ren and W. Song, *Small*, 2020, **16**, 1905083.
8. C. Fang, J. Zhou, L. Zhang, W. Wan, Y. Ding and X. Sun, *Nature Communications*, 2023, **14**, 4449.
9. J. Liu, H. Liu, H. Chen, X. Du, B. Zhang, Z. Hong, S. Sun and W. Wang, *Advanced Science*, 2020, **7**, 1901614.
10. G. Zhou, P. Wang, H. Li, B. Hu, Y. Sun, R. Huang and L. Liu, *Nature Communications*, 2021, **12**, 4827.
11. P. Guo, Z. Wang, T. Zhang, C. Chen, Y. Chen, H. Liu, M. Hua, S. Wei and X. Lu, *Applied Catalysis B: Environmental*, 2019, **258**, 117968.
12. M. A. Khan, H. Zhao, W. Zou, Z. Chen, W. Cao, J. Fang, J. Xu, L. Zhang and J. Zhang, *Electrochemical Energy Reviews*, 2018, **1**, 483-530.
13. H. Wang, K. H. Zhang, J. P. Hofmann and F. E. Oropeza, *Journal of Materials Chemistry A*, 2021, **9**, 19465-19488.
14. T. Tian, H. Gao, X. Zhou, L. Zheng, J. Wu, K. Li and Y. Ding, *ACS Energy Letters*, 2018, **3**, 2150-2158.
15. V. Vij, S. Sultan, A. M. Harzandi, A. Meena, J. N. Tiwari, W.-G. Lee, T. Yoon and K. S. Kim, *Acs Catalysis*, 2017, **7**, 7196-7225.
16. K. Zhu, X. Zhu and W. Yang, *Angewandte Chemie International Edition*, 2019, **58**, 1252-1265.
17. W. Zhu, W. Chen, H. Yu, Y. Zeng, F. Ming, H. Liang and Z. Wang, *Applied Catalysis B: Environmental*, 2020, **278**, 119326.
18. Q. Han, Y. Luo, J. Li, X. Du, S. Sun, Y. Wang, G. Liu and Z. Chen, *Applied Catalysis B: Environmental*, 2022, **304**, 120937.
19. C. Wang, H. Yang, Y. Zhang and Q. Wang, *Angewandte Chemie International Edition*, 2019, **58**, 6099-6103.
20. L. Zhao, J. Yan, H. Huang, X. Du, H. Chen, X. He, W. Li, W. Fang, D. Wang and X. Zeng, *Advanced Functional Materials*, 2024, **34**, 2310902.
21. Y.-C. Zhang, C. Han, J. Gao, L. Pan, J. Wu, X.-D. Zhu and J.-J. Zou, *Acs Catalysis*, 2021, **11**, 12485-12509.
22. X. Liu, W. Liu, M. Ko, M. Park, M. G. Kim, P. Oh, S. Chae, S. Park, A. Casimir and G. Wu, *Advanced Functional Materials*, 2015, **25**, 5799-5808.
23. A. Sumboja, J. Chen, Y. Zong, P. S. Lee and Z. Liu, *Nanoscale*, 2017, **9**, 774-780.
24. M. Sun and J. Wang, *Journal of Materials Chemistry A*, 2023, **11**, 21420-21428.
25. B. Liu, M. Zhang, Y. Wang, Z. Chen and K. Yan, *Journal of Alloys and Compounds*, 2021, **852**, 156949.

26. V. K. Magotra, A. Magotra, S. S. Mali, H. C. Jeon, T. W. Kang, A. S. Salunke, C. K. Hong, N. K. Shrestha, H. Im and A. I. Inamdar, *Membranes*, 2023, **13**, 748.

27. S. Zhang, B. Du, T. Li, J. Sun, Y. Meng, Z. Zhang and J. Kang, *Journal of Alloys and Compounds*, 2022, **900**, 163443.

28. A. Thomas, A. Kumar, G. Perumal, R. K. Sharma, V. Manivasagam, K. Popat, A. Ayyagari, A. Yu, S. Tripathi and E. Buck, *ACS Applied Materials & Interfaces*, 2023, **15**, 5086-5098.

29. M. Li, X. Deng, Z. Wang, K. Liu, Z. Ma, J. Wang and X. Wang, *Applied Surface Science*, 2022, **592**, 153328.

30. X. Sun, X. Sun, X. Liu, R. Liu, S. Li, M. Shen and Q. Li, *Results in Materials*, 2020, **5**, 100052.

31. L. Zhao, H. Zhang and B. Ma, *ACS omega*, 2023, **8**, 10503-10511.

32. H. Xiaobo, Y. Fengxiang, L. Yanhui, W. Hao, C. Jinnan, W. Yanhong and C. Biaohua, 2016.

33. C. Shi, J. Yu, Q. He, K. Liu, X. Li, W. Liu and M. Xu, *Journal of Nanoparticle Research*, 2021, **23**, 205.

34. Y. Wu, Y. Lu, C. Song, Z. Ma, S. Xing and Y. Gao, *Catalysis Today*, 2013, **201**, 32-39.

35. M. Aranda, P. Lavela and J. L. Tirado, *Battery Energy*, 2024, 20230057.

36. X. Pan, Z. Zheng, X. Zhang, X. He, Y. An, Y. Hao, K. Huang and M. Lei, *Engineered Science*, 2022, **19**, 253-261.

37. Y. Song, H. Liu, W. Dong and M. Li, *International Journal of Hydrogen Energy*, 2020, **45**, 4501-4510.

38. H. Wang, N. Mi, S. Sun, W. Zhang and S. Yao, *Journal of Alloys and Compounds*, 2021, **869**, 159294.

39. W. Wu, S. Liang, L. Shen, Z. Ding, H. Zheng, W. Su and L. Wu, *Journal of alloys and compounds*, 2012, **520**, 213-219.

40. S. M. Fawzy, M. M. Omar and N. K. Allam, *Solar Energy Materials and Solar Cells*, 2019, **194**, 184-194.

41. L. Wang, T. Yan, R. Song, W. Sun, Y. Dong, J. Guo, Z. Zhang, X. Wang and G. A. Ozin, *Angewandte Chemie International Edition*, 2019, **58**, 9501-9505.

42. Y. Wu, J. Lian, Y. Wang, J. Sun, Z. He and Z. Gu, *Materials & Design*, 2021, **198**, 109316.

43. B. Shen, X. Zhang, H. Ma, Y. Yao and T. Liu, *Journal of Environmental Sciences*, 2013, **25**, 791-800.

44. X. Shan, D. S. Charles, Y. Lei, R. Qiao, G. Wang, W. Yang, M. Feygenson, D. Su and X. Teng, *Nature communications*, 2016, **7**, 13370.

45. Q. Deng, X. Xia, M. Guo, Y. Gao and G. Shao, *Materials Letters*, 2011, **65**, 2051-2054.

46. W. Wang, L. Kuai, W. Cao, M. Huttula, S. Ollikkala, T. Ahopelto, A. P. Honkanen, S. Huotari, M. Yu and B. Geng, *Angewandte Chemie*, 2017, **129**, 15173-15177.

47. W.-M. Zhong, X.-G. Tang, Q.-X. Liu and Y.-P. Jiang, *Materials & Design*, 2022, **222**, 111046.

48. S. Zuo, Z. P. Wu, G. Zhang, C. Chen, Y. Ren, Q. Liu, L. Zheng, J. Zhang, Y. Han and H. Zhang, *Angewandte Chemie International Edition*, 2024, **63**, e202316762.

49. Z. P. Wu, H. Zhang, S. Zuo, Y. Wang, S. L. Zhang, J. Zhang, S. Q. Zang and X. W. Lou, *Advanced Materials*, 2021, **33**, 2103004.

50. M. Huynh, C. Shi, S. J. Billinge and D. G. Nocera, *Journal of the American Chemical Society*, 2015, **137**, 14887-14904.

51. Q. Liang, G. Brocks and A. Bieberle-Hütter, *Journal of Physics: Energy*, 2021, **3**, 026001.

52. I. C. Man, H. Y. Su, F. Calle-Vallejo, H. A. Hansen, J. I. Martínez, N. G. Inoglu, J. Kitchin, T. F. Jaramillo, J. K. Nørskov and J. Rossmeisl, *ChemCatChem*, 2011, **3**, 1159-1165.

53. J. Song, C. Wei, Z.-F. Huang, C. Liu, L. Zeng, X. Wang and Z. J. Xu, *Chemical Society Reviews*, 2020, **49**, 2196-2214.

54. Y.-F. Li and A. Selloni, *Acs Catalysis*, 2014, **4**, 1148-1153.

55.   D. Wu, X. Shen, X. Liu, T. Liu, Q. Luo, D. Liu, T. Ding, T. Chen, L. Wang and L. Cao, *The Journal of Physical Chemistry C*, 2021, **125**, 20301-20308.
56.   C. Zhang, Z. Xie, Y. Liang, D. Meng, Z. Wang, X. He, W. Qiu, M. Chen, P. Liang and Z. Zhang, *International Journal of Hydrogen Energy*, 2021, **46**, 17720-17730.
57.   Z. Li, X. He, Q. Qian, Y. Zhu, Y. Feng, W. Wan and G. Zhang, *Advanced Functional Materials*, 2023, **33**, 2304079.
58.   S. Liu, L. Liu, Z. Cheng, J. Zhu and R. Yu, *The Journal of Physical Chemistry Letters*, 2021, **12**, 5675-5681.
59.   V. Maruthapandian, T. Pandiarajan, V. Saraswathy and S. Muralidharan, *RSC advances*, 2016, **6**, 48995-49002.
60.   P. Nagajyothi, R. Ramaraghavulu, K. Munirathnam, K. Yoo and J. Shim, *International Journal of Hydrogen Energy*, 2021, **46**, 13946-13951.
61.   C. C. Gowda, A. Mathur, A. Parui, P. Kumbhakar, P. Pandey, S. Sharma, A. Chandra, A. K. Singh, A. Halder and C. S. Tiwary, *Journal of Industrial and Engineering Chemistry*, 2022, **113**, 153-160.
62.   G. Henkelman, B. P. Uberuaga and H. Jónsson, *The Journal of chemical physics*, 2000, **113**, 9901-9904.
63.   K. Zhang and R. Zou, *Small*, 2021, **17**, 2100129.
64.   H. Jung, S. Choung and J. W. Han, *Nanoscale Advances*, 2021, **3**, 6797-6826.
65.   A. Grimaud, O. Diaz-Morales, B. Han, W. T. Hong, Y.-L. Lee, L. Giordano, K. A. Stoerzinger, M. T. Koper and Y. Shao-Horn, *Nature chemistry*, 2017, **9**, 457-465.
66.   P. Ye, K. Fang, H. Wang, Y. Wang, H. Huang, C. Mo, J. Ning and Y. Hu, *Nature Communications*, 2024, **15**, 1012.
67.   X. Wang, S. Xi, P. Huang, Y. Du, H. Zhong, Q. Wang, A. Borgna, Y.-W. Zhang, Z. Wang and H. Wang, *Nature*, 2022, **611**, 702-708.

Data Availability: Data are available upon request from the authors